Study on the influence of measured geometric shape deviations on the deformation capacity and post buckling behavior of hollow sections loaded in compression and bending

Andreas Müller[1], Andreas Taras[2],

Abstract
In international design codes on the design of steel structures, the maximum rotational capacity of a section is limited and linked to the definition of cross-sectional classes. For example, in Eurocode 3, class 2 cross-sections are defined as sections that can reach their plastic moment, but fail to reach a rotation capacity of $R_{cap}=3$, while Class 1 cross-sections fulfil this demand. Eurocode 8 (seismic design) gives deformation capacity limits for limit states analysis of existing structures and limited by the condition that the normalized axial load is lower than 0,3. The classification of cross-sections necessarily leads to discontinuities in the representation of both strength and deformation capacities. This paper illustrates first steps towards an alternative approach that makes use of a continuous definition of deformation capacities in dependence of cross-sectional slenderness values. In the case of the rotation capacity in bending, recently conducted tests on hot rolled and cold finished SHS hollow sections made of mild and high-strength steel grades showed that the choice of different eigenmode-based pre-buckling shapes as initial imperfections for geometrically and materially non-linear (GMNIA) calculations lead to near identical values of the reached maximum moment, yet show significant variation in the post-buckling paths. A comparative FEM based evaluation of surface-scan-based real geometry models also showed variability in the post-buckling behavior as well as different plastic hinge formation spots. This paper presents a thorough look on the effect of different theoretical and measured, scanned imperfection shapes on the post-buckling behavior of SHS and RHS hollow sections.

1. Introduction

Structural hollow sections have a wide range of engineering applications, especially when the need for high structural efficiency, self-weight optimization architecturally pleasing structural solutions arise. Two main manufacturing processes are employed in their fabrication, i.e. cold-forming or seamless hot-forming (EN 10210-2 2006; EN 10219-2 2006) which also lead to the main differences in material properties (Yun 2018; Gardner 2010; Amouzegar 2016; Ma 2015) and residual stresses (Gardner 2010; Ma 2015; Kato 1982; Tong 2012; Abvabi 2015; Zhang 2010).

---

[1] PhD. Student, ETH Zurich, Institute of Structural Engineering, <andreas.mueller@ibk.baug.ethz.ch>
[2] Professor – Steel and Composite Structures, ETH Zurich, Institute of Structural Engineering, <ataras@ethz.ch>

For the use of inelastic analysis methods, the structural members must have a certain amount of ductility to undergo deformation after reaching its initial yield without any significant loss in its ultimate strength. This rotation capacity R_{cap} is defined through Eq. (1). It is a measure of how much the plastic hinge can rotate before failure occurs. Thereby, φ represents the beam end sections' rotation and its limit values φ_{pl}, φ_u, $\varphi_{pl,2}$ (see Figure 1). The rotation $\varphi_{pl,2}$ is defined as rotational angle in a deformation-driven test or analysis at which the moment drops below M_{pl}. EC3-1-1 (EN 1993-1-1 2005) provides rotation demands R_{cap} depending on the cross-section classifications. According to this definition, class 2 cross-sections can reach its plastic moment, but fail to reach a rotation capacity of 3. Class 1 cross-sections fulfil this demand by reaching a rotation capacity that is larger than 3, see Figure 1a. Although the code considers only a minimum permitted rotation capacity for the sections ($R_{cap} = 3$), the actual rotation capacity of a structural member could be determined more accurately by means of FEM-based plastic analysis.

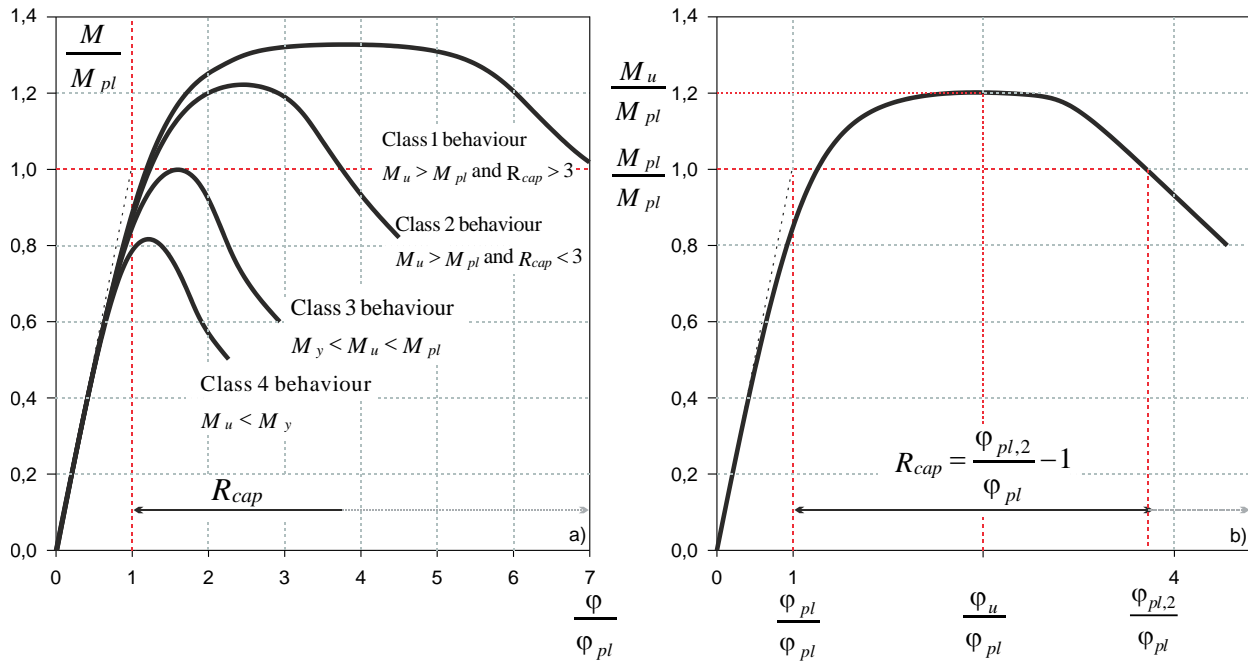$$P_{cap} = \frac{\varphi_{pl,2} - \varphi_{pl}}{\varphi_{pl}} = \frac{\varphi_{pl,2}}{\varphi_{pl}} - 1 \tag{1}$$

Figure 1: Rotation capacity Rcap as function of cross-sectional classes in accordance with EC3-1-1 (2005); b) Definition of the Rotation capacity Rcap

Considerable effort was placed for some time on defining parameters that effect the rotation capacity. Saloumi (2016) recently gave a good outline of quantification and sensibility factors regarding the rotation capacity: (i) the identification of a strength reserve after local buckling (Luckey 1969); (ii) the identification of three governing parameters for the rotation capacity of I-shaped sections – flange slenderness as a key parameter, the web stiffness and the steepness of the moment gradient (Kuhlmann 1989); (iii) Investigations in (Kuhlmann 1989; Stranghöner 1994; Ricles 1998) led to the conclusion that the degree of strain hardening significantly influences the rotation capacity; and (iiii) a significant influence of initial imperfections on the moment-rotation curve, the plastic hinge formation and the post buckling behavior in the decreasing part was

observed in (Boeraeve et.al., 1993) and can be confirmed by first preliminary investigations on SHS profiles (Müller and Taras 2019a).

With the advent of better measurement methods supported by new technologies, the possibilities for more precise evaluation arise. Where a few years ago imperfection measurements had to be made laboriously by hand, containing only a limited number of selected points, the use of scanners lead to a non-contact, precise and relatively easy recording method of imperfections resulting in full scale 3D-surface scans. This relatively new method was already applied successfully in different projects e.g. (McAnallen et.al., 2014), (Sadowski et.al., 2015) as part of an EU RFCS project "Combitube" for the evaluation of imperfections of spiral-welded steel tubes but also by (Müller et.al., 2018) and (Müller and Taras 2019d) in the outline of two industrial projects conducted at the University of Bundeswehr Munich, in order to evaluate the load bearing capacity and the influence of imperfections of spiral-welded aluminum tubes.

Within the framework of the EU-funded (Research Fund for Coal and Steel) research project "Hollosstab" – which aimed at developing innovative buckling design rules for slender structural hollow sections made of high-strength steel and conventional or custom-made cross-sectional shapes (Toffolon et al. 2019a) – all specimens were scanned beforehand as part of the experimental campaign, providing one of the largest 3D-surface scan databases on cold formed and hot rolled hollow section to date. The collected 3D-surface scan data form the basis for further investigations on imperfections and its influence on the post-buckling behaviour. In a first initial step the influence of imperfections, based on 3D scan data and additional Geometrically and Materially Non-linear Analyses with Imperfections (GMNIA), was investigated in order to show differences in the development of the plastic hinge location and its impact on the resulting post-buckling curves (Müller and Taras 2019b). It was shown that initial imperfections have an influence on the post-buckling path and the location of the plastic hinge (see Section 4.1). To get a more precise look at the imperfection within one specimen, it is necessary to implement advanced methods, which allow a manipulation and reconstruction of the scanned 3D-surface. This paper presents a "surface development method" based on Fourier series expansion to analyse the range of imperfections within one specimen, reconstruct and detect the minimum needed amount of imperfections to describe an approximate surface giving a sufficient prediction regarding the maximum load but also the rotation and displacement resulting from finite element calculations. Similar approaches were also adopted by (Ding et.al., 1996), (Teng et.al., 2005) and (Sadowski et.al., 2015), respectively. Nevertheless, this method has so far been used for the imperfection analysis of cylindrical silos and spiral welded steel tubes of large diameter, not for RHS and SHS hollow sections conducting additional FE calculations based on the reconstructed 3D-surfaces.

In the context of this paper, the EU RFCS project "Hollosstab" is not presented in detail. Further information on the experimental campaign, the developed design rules regarding the new **G**eneralized **S**lenderness bases **R**esistance **M**ethod (G.S.R.M), providing a continuous formulation of the resistance throughout the slenderness, and additional proceedings are listed as follows (Toffolon et.al., 2019a; Toffolon et.al., 2019b; Toffolon 2019c; Toffolon 2019d; Meng et.al., 2019). The summarized project overview can also be seen in (steelconstruct 2019).

2. Imperfection measurement, assessment and reconstruction

2.1 Reverse Engineering procedure

Test specimen	Point cloud	Spline surface	FE-Model

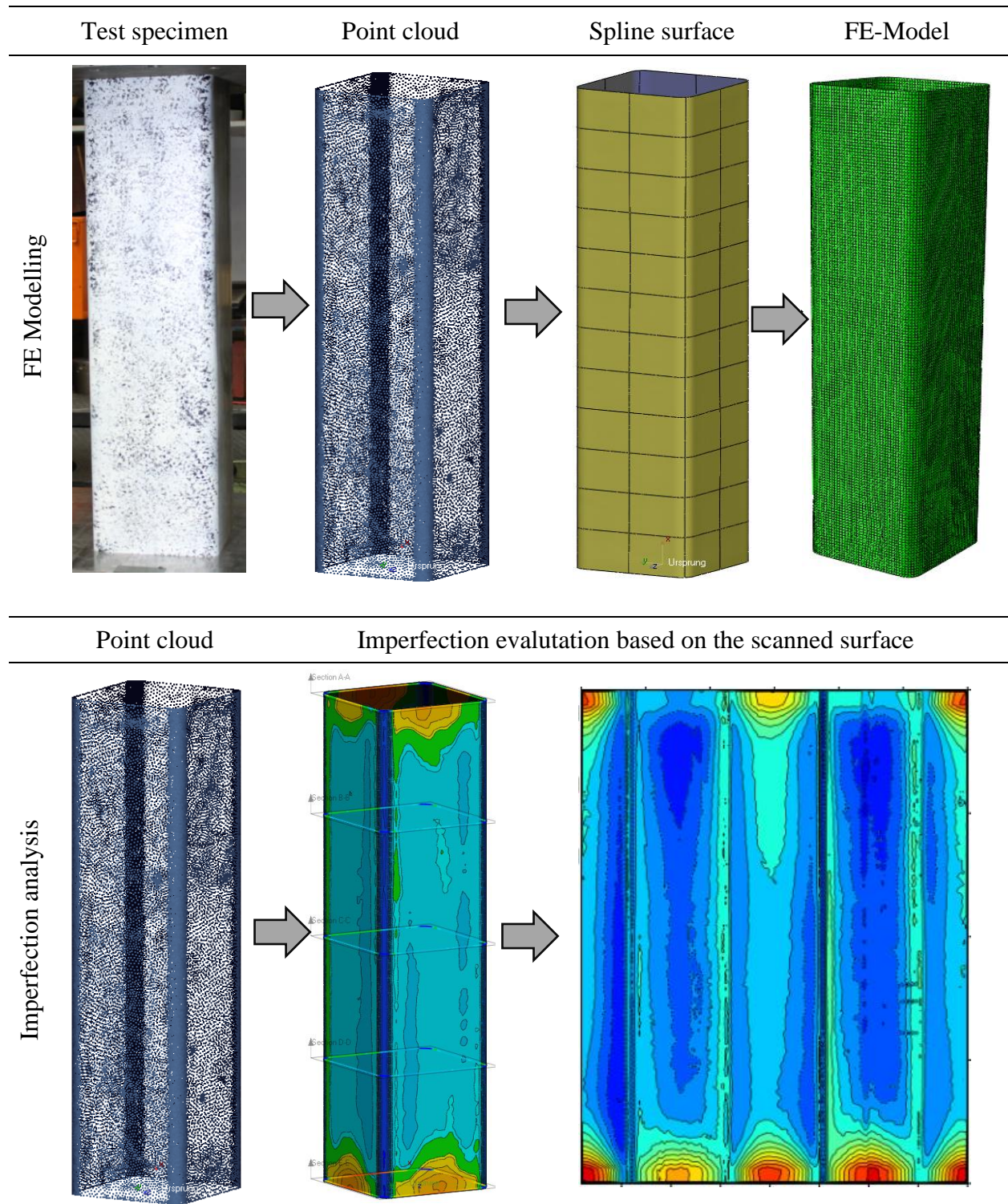| Point cloud	Imperfection evalutation based on the scanned surface

Figure 2: Applied reverse engineering workflow scheme

The Reverse Engineering Workflow shown in Fig.2 is splitted in two main procedures, depending on the desired result and the necessity. The Finite Element Modelling, as the first procedure, requires a scanned point cloud obtained from the test specimen using an optical 3D digitizing system, which symbolizes the raw data. In order to use the scanned point cloud as the later finite element model an intermediate step is necessary, where a spline surface need to be generated. This step can easily be achieved by appropriate software like Geomagic Control X or CloudCompare. The real specimen geometry can subsequently be implemented into a FE based program in order to evaluate the laboratory test and assess the imperfections. This approach was already tested and performed successfully by (Müller and Taras 2017, Müller and Taras 2019d) and (Toffolon et.al., 2019a). However, a more detailed analysis of imperfection was never conducted, as it was not the prior focus.

The effective imperfections of the real specimen geometry can be determined by using the scanned-surface data and compare it with a CAD-Model of perfect nominal geometry. This step symbolizes the initial imperfection analysis and gives an overview of the imperfections along the specimen (see Fig. 3). On this analysis level, it is rather inaccurate to discuss about e.g. local imperfections as effects like sagging and ovalization affect these and are inherent to the sum of all imperfections within one specimen. To eliminate these effects or even being able to pick different "modes" out of the imperfection spectrum it is necessary to make additional steps that commercial software does not know. A thorough look on this issue gives Section 2.2.
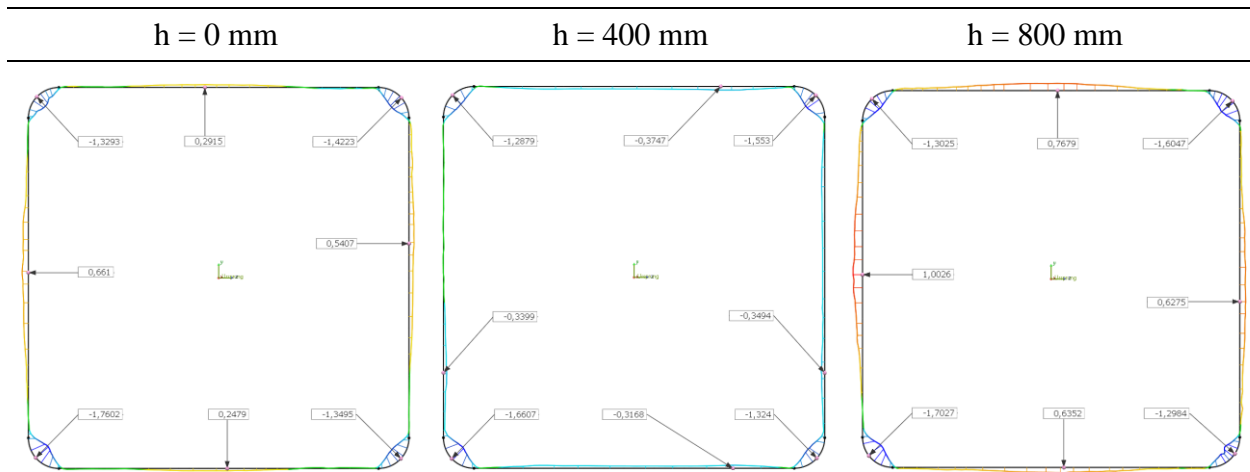
h = 0 mm	h = 400 mm	h = 800 mm

Figure 3: Imperfection evaluation of a SHS 200*200*5 profile along the height (h = 800 mm)

2.2 Surface reconstruction based on Fourier Series Expansion
The steps described in Section 2.1 lead to an overall imperfection evaluation giving the deviation between the scanned and the perfect surface as an output. This "prepared" data is used as an input file for a python script developed at the ETH Zurich, Institute of Structural Engineering (IBK) Steel- and Composite Structures. Where the imperfection data of the considered specimen is first transformed or mapped to a flat surface by "unfolding" the hollow section. Using than the Python griddate command allows the implementation of a uniformly-spaced x(Height)-y(Circumference) grid (see Fig.4, top). Subsequently, by applying a 1D full wave Fourier series expansion (see Eq. 2) and calculating an arbitrary number of harmonic numbers for the Fourier coefficients an imperfection spectrum for the given specimen is obtained (see Fig.4, bottom). Low harmonic

numbers between 0 and 3 are usually related to global sagging and ovalization, whereas higher harmonic numbers are used to reconstruct local imperfections (Sadowski et.al., 2015; Müller and Taras 2019).

$$w(x, y) = \sum_{k=0}^{K} \left(a_k(y) \cdot \cos\left(2 \cdot \pi \cdot k \cdot \frac{x}{x_{max}} \right) + b_k(y) \cdot \sin\left(2 \cdot \pi \cdot k \cdot \frac{x}{x_{max}} \right) \right) \qquad (2)$$

with:

$$a_0 = \frac{1}{2L} \int_{xn}^{xn+1} f(x)\,dx; \quad a_k = \frac{1}{L} \int_{xn}^{xn+1} f(x) \cdot \cos\left(\frac{n\pi x}{L} \right) dx \qquad (3)$$

$$b_k = \frac{1}{L} \int_{xn}^{xn+1} f(x) \cdot \sin\left(\frac{n\pi x}{L} \right) dx \qquad (4)$$
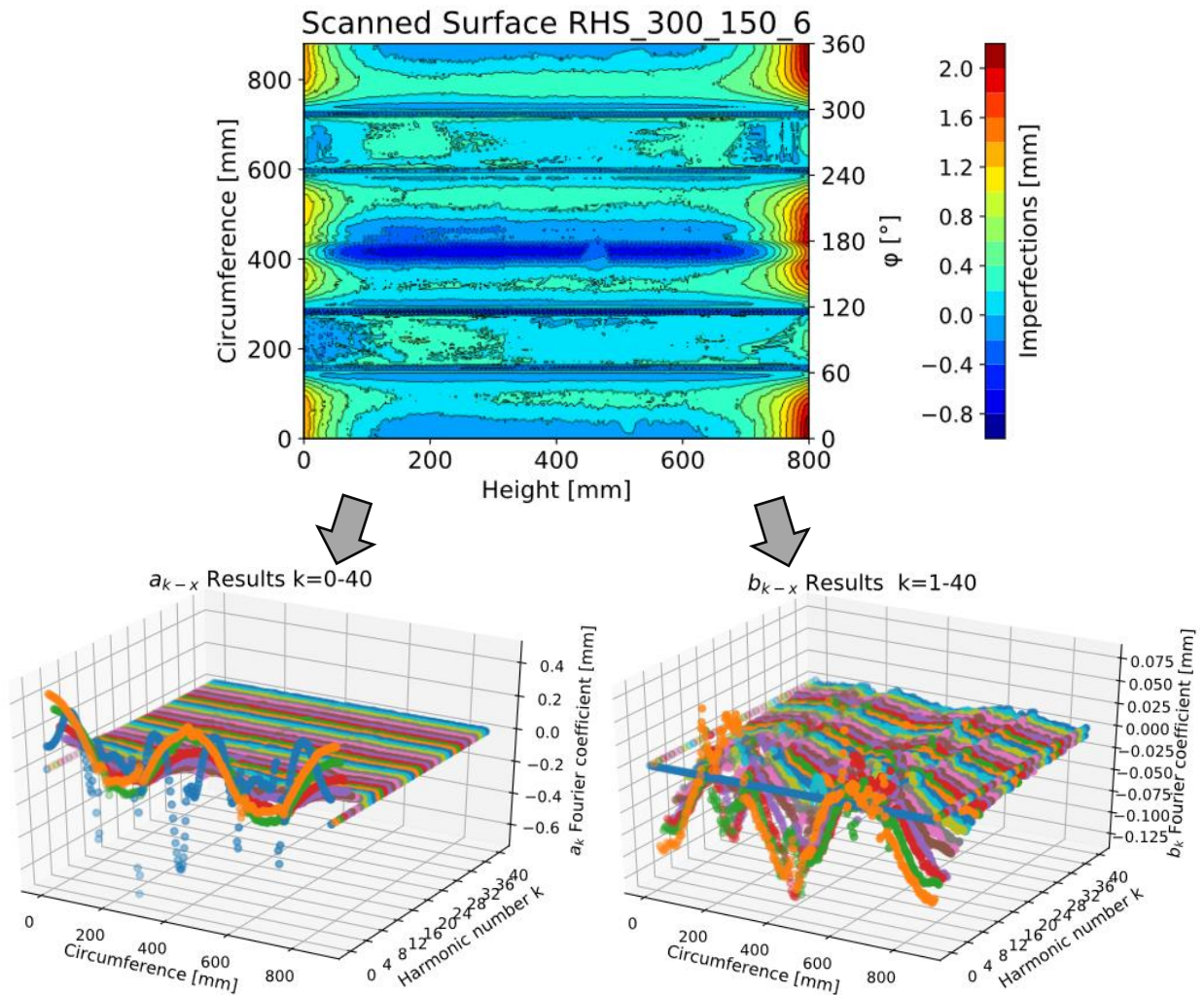
$$f(x) = mx + t \qquad (5)$$

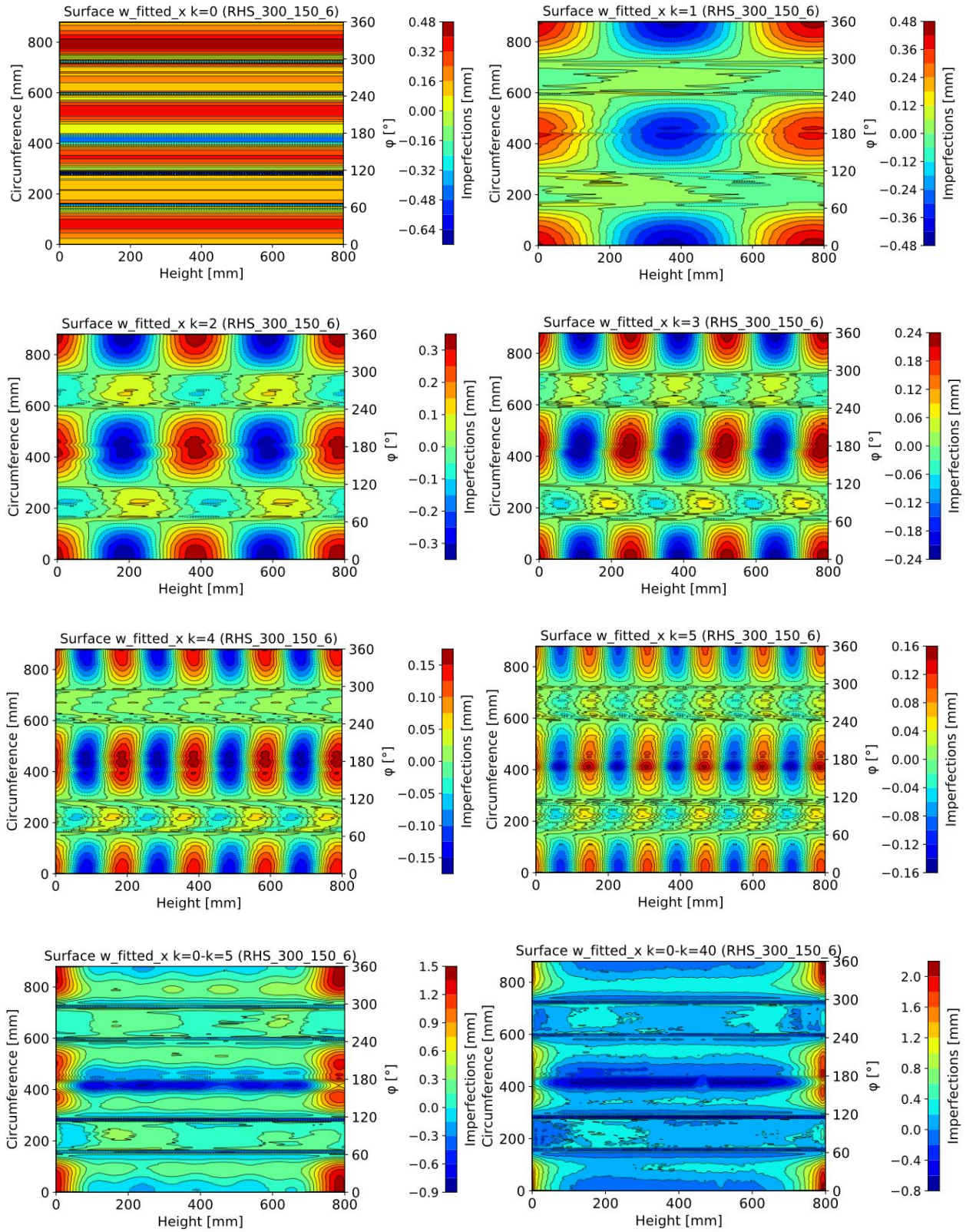Figure 4: Calculated Fourier coefficients a_k and b_k for a RHS 300*150*6

Figure 5: Reconstructed surfaces depending on different Fourier coefficients

Figure 5 shows in the upper first three lines the reconstructed surfaces using the Fourier coefficients from 0 to 5 one by one separately. The bottom line of Figure 5 displays the sum of the reconstructed surfaces for the Fourier coefficients from 0 to 5 on the left and from 0 to 40 on the right side, leading to an increasingly precise surface approximating the original scanned surface. Calculating the coefficient of variation (cov) between the reconstructed and the scanned surface for a rising harmonic numbers leads logically to the same assumption of an increasing similarity; $cov_{k0-k0} = 1.24\%$, $cov_{k0-k1} = 0.92$, $cov_{k0-k2} = 0.70$, $cov_{k0-k3} = 0.53$, $cov_{k0-k4} = 0.41$, $cov_{k0-k5} = 0.32$, $cov_{k0-k10} = 0.14$, $cov_{k0-k40} = 0.63 \cdot 10^{-2}$. The harmonic number 0 gives, due to its mathematical formulation, an average of the imperfections over the height of the specimen, remaining constant along the height. Toward higher numbers also the harmonic amplitude increases describing the effects already mentioned above e.g. sagging, ovalization and local dimple imperfections.

3. Numerical Modelling

A series of individual calculation runs of increasing sophistication were performed in the numerical studies presented in this paper. Linear bifurcation analyses (LBA) were carried out in order to identify the elastic critical buckling resistance. Geometrically and materially nonlinear analyses (GMNA) served the purpose of identifying the elastic-plastic buckling resistance of the perfect structure. Geometrically and materially nonlinear analyses with imperfections (GMNIA) were performed to determine the elasto-plastic buckling load, i.e. the realistic buckling resistance that considers both material and geometric nonlinearities. For the calculations based on the scanned real geometry data, no further analysis types – like LBA or GMNA – had to be performed beforehand and a GMNIA could directly be performed on the as-fabricated structural geometry. This calculation served as a means to calibrate and validate the numerical model against the conducted full-scale tests.

For the numerical analysis, two recently published material models for hot-rolled and cold-formed steel grades were considered, with the aim of describing the structural behaviour with increased accuracy. The employed material model for hot-rolled carbon steel is based on a bilinear plus non-linear hardening description (Yun 2018) and consists only of three parameters E, f_y and f_u. It can be summarized as follows:

$$f_{(\varepsilon)} = \begin{cases} E \cdot \varepsilon & \text{for } \varepsilon \le \varepsilon_y \\[2em] f \cdot y & \text{for } \varepsilon_y \le \varepsilon \le \varepsilon_{sh} \\[2em] f_y + (f_u - f_y)\left[0.4\left(\dfrac{\varepsilon - \varepsilon_{sh}}{\varepsilon_u - \varepsilon_{sh}}\right) + \dfrac{2\left(\dfrac{\varepsilon - \varepsilon_{sh}}{\varepsilon_u - \varepsilon_{sh}}\right)}{\left[1 + 400\left(\dfrac{\varepsilon - \varepsilon_{sh}}{\varepsilon_u - \varepsilon_{sh}}\right)^5\right]^{\frac{1}{5}}}\right] & \text{for } \varepsilon_{sh} \le \varepsilon \le \varepsilon_u \end{cases} \tag{6}$$

The stress-strain response for the considered cold-formed steel grades S355 and S700 can be described by a two-stage Ramberg-Osgood model [3], as summarized in Eq. (5) and Table 2 below. The fact that cold-formed steel shows a different stress-strain relation in the corner and flat areas, as well as the overall presence of residual stresses, were not taken into account in the calculations

for this paper, as the investigations in (Yun 2017) determined that these stress-strain relations may accurately describe the cross-sectional behaviour in an average sense, including the combined effects of modified stress-strain curves in the corners and the resulting residual stresses.

$$\varepsilon = \begin{cases} \dfrac{f}{E} + 0.002\left(\dfrac{f}{f_y}\right)^n & \text{for } f \leq f_y \\[4mm] \dfrac{f-f_y}{E_{0.2}} + \left(\varepsilon_u - \varepsilon_{0.2} - \dfrac{f_u-f_y}{E_{0.2}}\right)\cdot\left(\dfrac{f-f_y}{f_u-f_y}\right)^m + \varepsilon_{0.2} & \text{for } f_y \leq f \leq f_u \end{cases} \tag{7}$$

Finally, the implementation of the material model in the FEM software Abaqus (Abaqus 2016) required the translation of engineering stress-strain values (σ_{eng}, ε_{eng}) into true stress-strain values (see Eq. (8) and (9)):

$$\varepsilon_{true} = \ln\left(1 - \varepsilon_{eng}\right) \tag{8}$$

$$\sigma_{true} = \sigma_{eng}\left(1 - \varepsilon_{eng}\right) \tag{9}$$
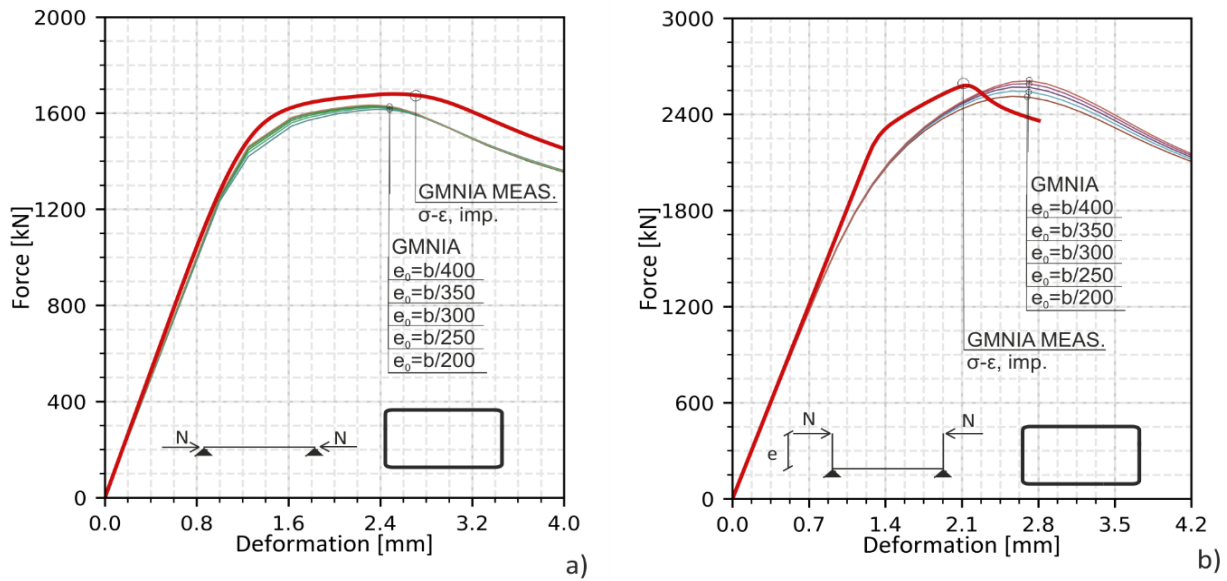

Figure 6: Comparison between the GMNIA_Meas and calibrated GMNIA calculations based on LBA-Eigenmode imperfections (Toffolon and Taras 2019d)

The employed numerical models made use of three-dimensional shell elements of type S4R and the above-mentioned material models bases on the publication by (Yun 2013; Yun 2017). The verification and validation of the numerical models is based on the conducted laboratory tests, which were performed in the context of the EU-funded (RFCS) project HOLLOSSTAB (Grant Nr. 2015-709892). The scanned 3D-surface models (GMNIA_Meas) were used to represent the real

tests as good as possible, as all initial imperfections were present. Models for additional parameter studies were calibrated to these 3D-surface models by using adjusted LBA-Eigenmode imperfections, exclusively used for the development of the GSRM method during the exhibition of the HOLLOSSTAB project. As these models are adopted to the purpose of a resistance-based method, the prediction of the maximum load is precisely, but not that of the displacement (see Fig. 6). The results presented in this paper are based on the scanned surface models that were developed by the Reverse Engineering workflow declared in Section 2.1.

4. Effects of initial Imperfection on the post-buckling behavior

4.1 Preliminary investigations on the post-buckling behavior

Preliminary investigations in (Müller and Taras 2019c) showed an impact of initial imperfections on the post-buckling behaviour, both by assuming different eigenmode based imperfections in additional GMNIA calculations and by using FE-models evaluated on the real geometry of the tested specimens by a 3D-scanning procedure.

In the first case, a square hollow section with 200mm depth (SHS 200) was used to perform calculations using different LBA-eigenmode based imperfections. The thickness varied between the values of 2mm to 16mm to serve the purpose of illustrating the general behaviour of a full range of sections, from thick-walled and stocky to very thin-walled. The steel grade S355 and the specimen length were set constant, whereas to manufacturing processes of hot rolling and cold forming were considered. Through the study, the models were loaded by a constant rotation at both ends of the specimen. To illustrate the imperfection sensitivity throughout the various slenderness ranges, the coefficient of variation (cov) of the rotation capacity was calculated for every examined thickness and plotted against the slenderness. Figure 7 shows a summary of all calculations, with the cov's as well as the corresponding cross-section classes.
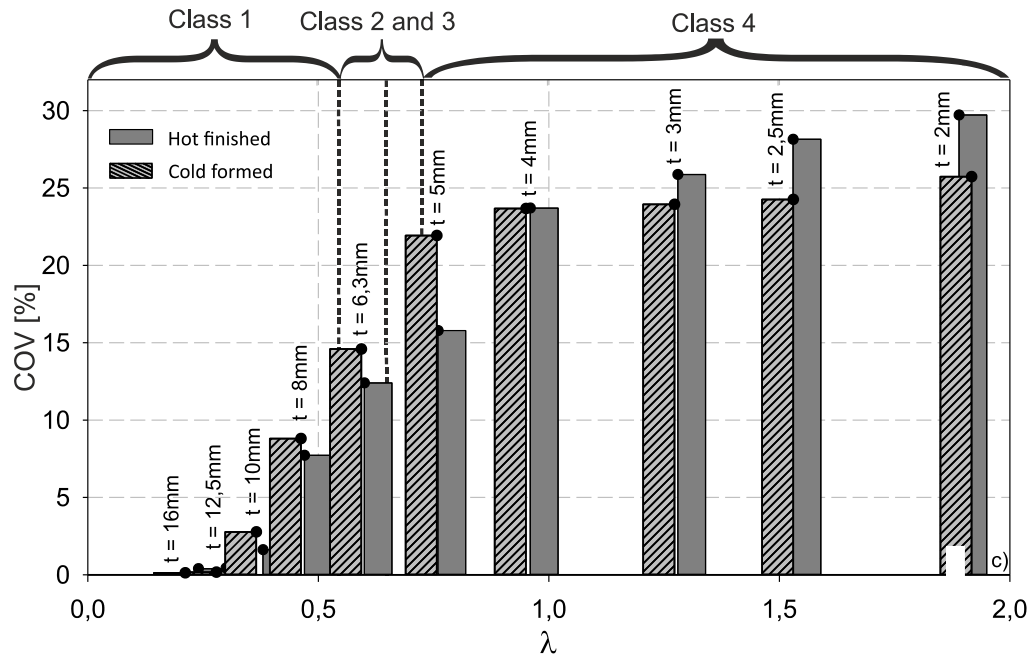

Figure 7: Coefficient of Variation [%] of the deformation capacity of various S355 – SHS200 sections, as function of the plate slenderness $\lambda = (c/t) / \left(28.4 \cdot \varepsilon \cdot \sqrt{k_\sigma}\right)$, see EC3-1-5.

The cov for the thickest cross-section with t = 16 mm is also the lowest, $cov_{16mm} = 0{,}40$ for hot-rolled and $cov_{16mm} = 0{,}13$ for cold formed steel. Starting from this value towards a higher slenderness the covs increase, reaching their maximum for t = 2 mm, with $cov_{2mm} = 30$ for hot-rolled and $cov_{2mm} = 26$ for cold formed steel. In summary, the graphs indicate that with rising slenderness of compact SHS sections the scatter of the post buckling curves for different imperfection shapes increases disproportionally. Wilkinson (1999) also found out that the magnitude of the imperfection had an unexpectedly significant impact on the rotation capacity, studied in this case for stockier sections.

To substantiate the assumptions of variations of imperfection shapes and amplitudes within one specimen, an evaluation for cold-formed SHS profiles is shown in Fig. 8. The rotation is read in each case at the top and the bottom of the specimen, as the post buckling path is highly dependent on the location of the local buckling area in all analyses that are based on real, measured geometric imperfections. This means that, contrary to GMNIA calculations based on theoretical imperfection shapes based on LBA eigenmodes, real post-buckling deformations are sensitive in their behaviour even with respect to the precise location of the first plastic hinge, further complicating any prediction. If the local buckling field is assumed at the top, the corresponding rotation of the top boundary will also be higher compared to the rotation at the bottom. By looking at side z- of Fig. 7a, buckling appeared in the upper area. Therefore, rotation at the top boundary leads to a pronounced post buckling path with a soft subside. However, plotting the rotation of the bottom boundary leads to a sharp kink in the post buckling path. The opposite is valid for side y+, where buckling appeared at the bottom of the specimen. Additional calculations for two RHS profiles of equal dimensions were performed in the context of this paper to show the same influences on the post-buckling behavior as for SHS profiles (see Fig. 9).
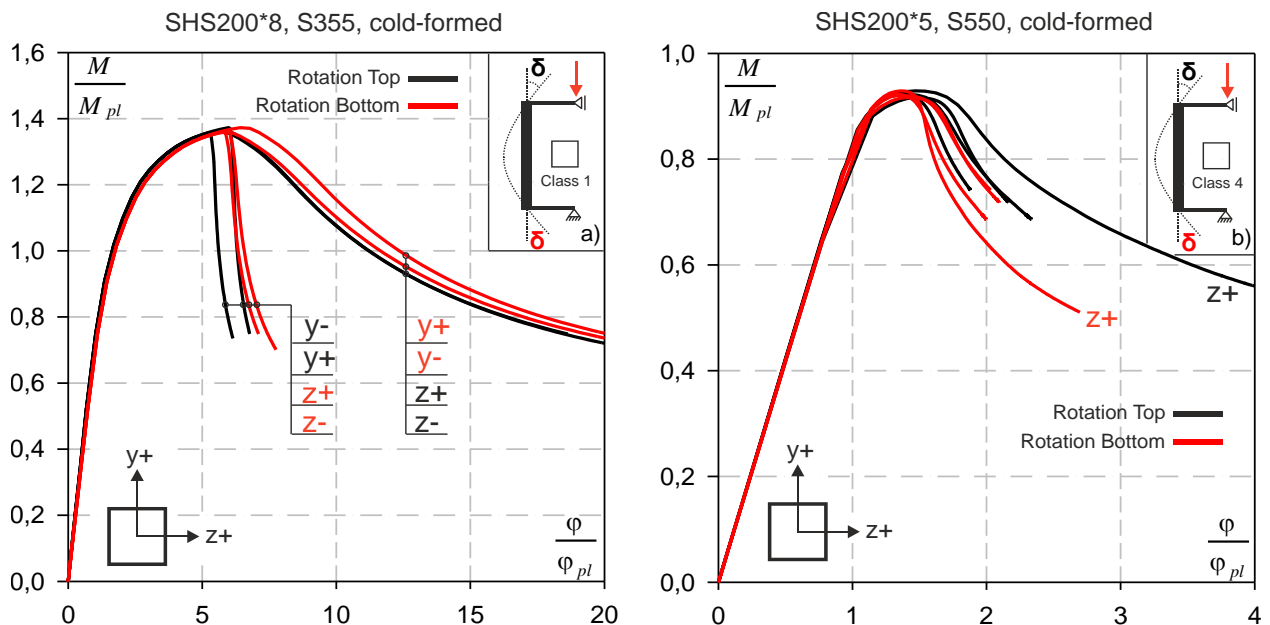

Figure 8: Moment-rotation-relations for each side of the SHS200*8mm (S355) and SHS200*5mm (S550) profile
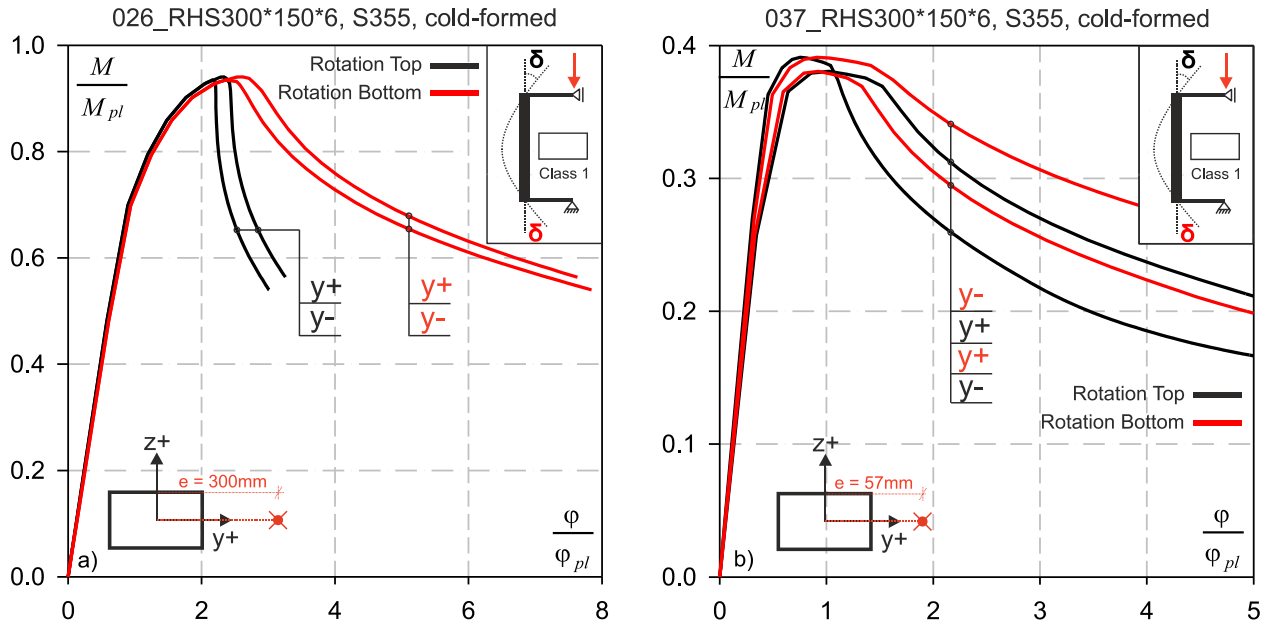
Figure 9: Moment-rotation-relations for the positive and negative y-direction of the 026_RHS300*150*6mm (S355) and 037_RHS300*150*6mm (S355) profile

4.2 Detailed investigations on the post-buckling behavior

Using the technique described in Section 2.2 brings a useful advantage on handling the data compared to the raw scanned surface, as this step does not provide the opportunity of discretizing the finite element mesh of the model. By first "gridding" the surface, as an intersection step, gives one this additional opportunity making the reverse engineering process more controllable. In order to verify the accuracy of the Fourier based modelling method, GMNIA calculations were performed by using different Fourier coefficients with ascending harmonic number from 0 to 40.
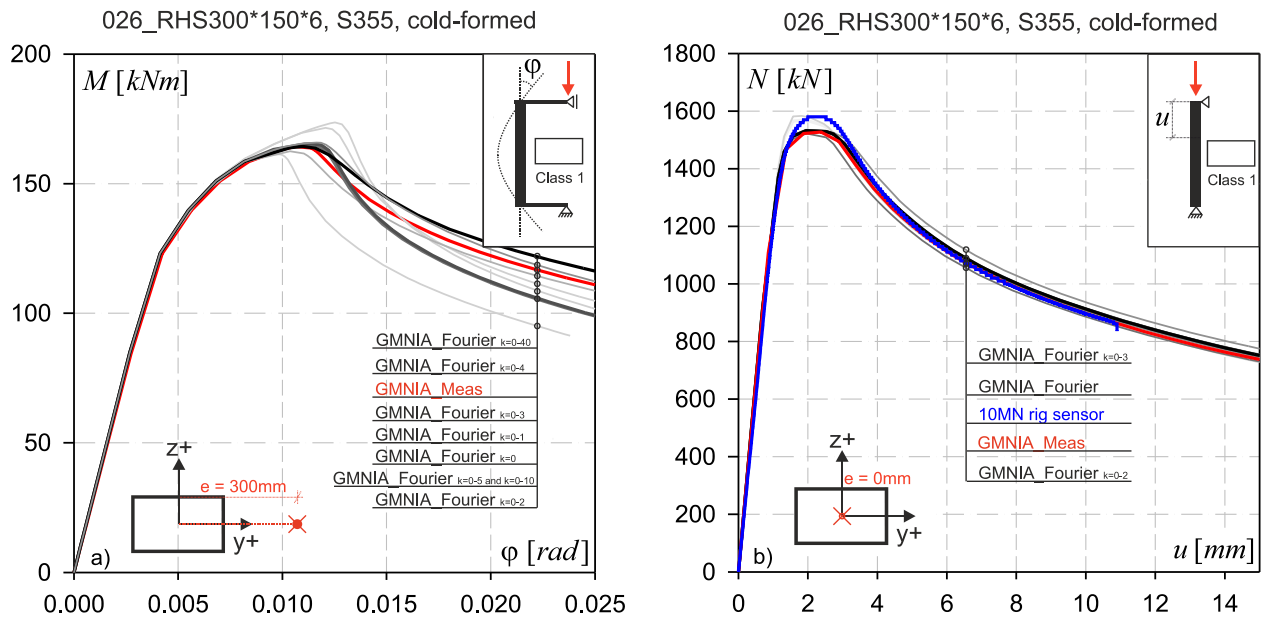

Figure 10: Verification of the Fourier based modelling technique

12

Tested Specimen	GMNIA_MEAS	GMNIA_Fourier (k=40)

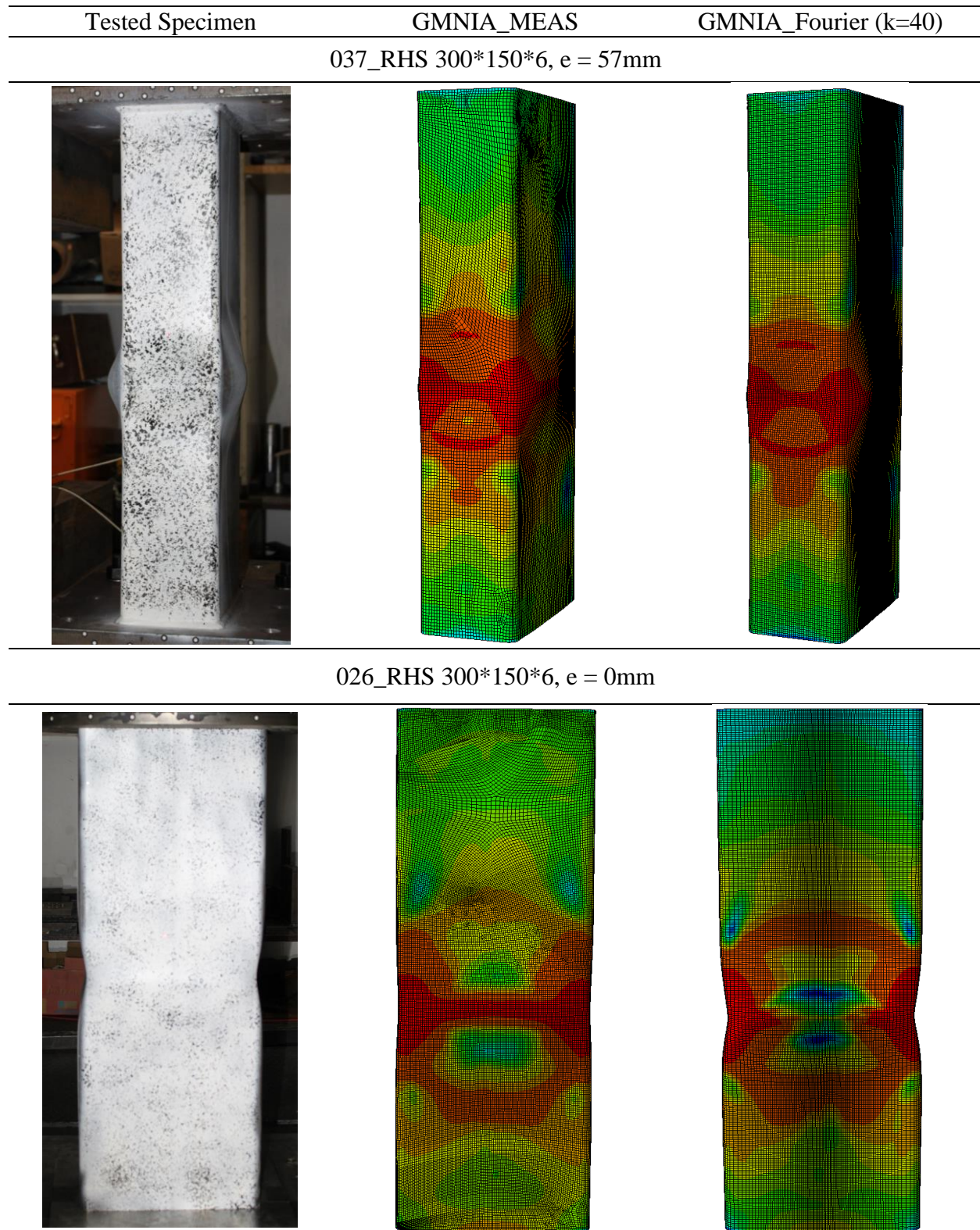### 037_RHS 300*150*6, e = 57mm

026_RHS 300*150*6, e = 0mm

Figure 11: External comparison of buckling shapes between Tested Specimen, GMNIA_Meas and GMNIA_Fourier

Figure 10 summarizes an exemplary evaluation of the reconstruction method regarding the minimum needed amount of harmonic numbers in order to imitate the scanned surface to the extent necessary. Shown on the left side a load-displacement diagram of a centrically loaded and on the right side a moment-rotation diagram of an eccentrically loaded RHS profile. It has been shown that good accuracy is already achieved by applying the first four harmonic numbers for the reconstruction of the surface in case of the centric load (Fig.10b). In case of the eccentrically loaded profile (Fig. 10a) the scatter in the post-buckling moment-rotation relation is higher compared to Fig. 10b. However, the accuracy improves with a rising harmonic number. The worst results are predicted for the reconstructed models with the harmonic number from k = 0 to k = 3. Up to the harmonic number of k = 40 the moment-rotation curve adopts to that calculated from the 3D scanned surface (GMNIA_Meas). An additional comparison between the buckling shapes of the tested specimen, a GMNIA_Meas and a GMNIA_Fourier calculation is illustrated exemplary in Figure 11 for two different RHS profiles with equal dimensions. At this point, it must be pointed out that further calculations with additional profiles are required to confirm the accuracy of this method. In fact, the required accuracy, thus the sum of needed harmonic numbers depend on the load scenario, comparable with load-dependent eigenvalues based on LBA calculations. Sadowski (2015) described that the critical terms in the harmonic analysis are usually not those with the largest amplitudes (typically low harmonics), but those with wavelengths close to that of the critical buckling mode (typically a high harmonic).

In order to further corroborate this assumption, additional calculations were performed, where the harmonic numbers from k=0 to 5 were considered separately to reconstruct, in each case, an imperfect surface based on just one individual harmonic number. This consideration allows one to identify a "weighting factor" for different imperfections and also recognize crucial form within a bigger range of imperfections. This was done for the centric as well as the eccentric load case, summarized in Fig. 12a and Fig. 12b.
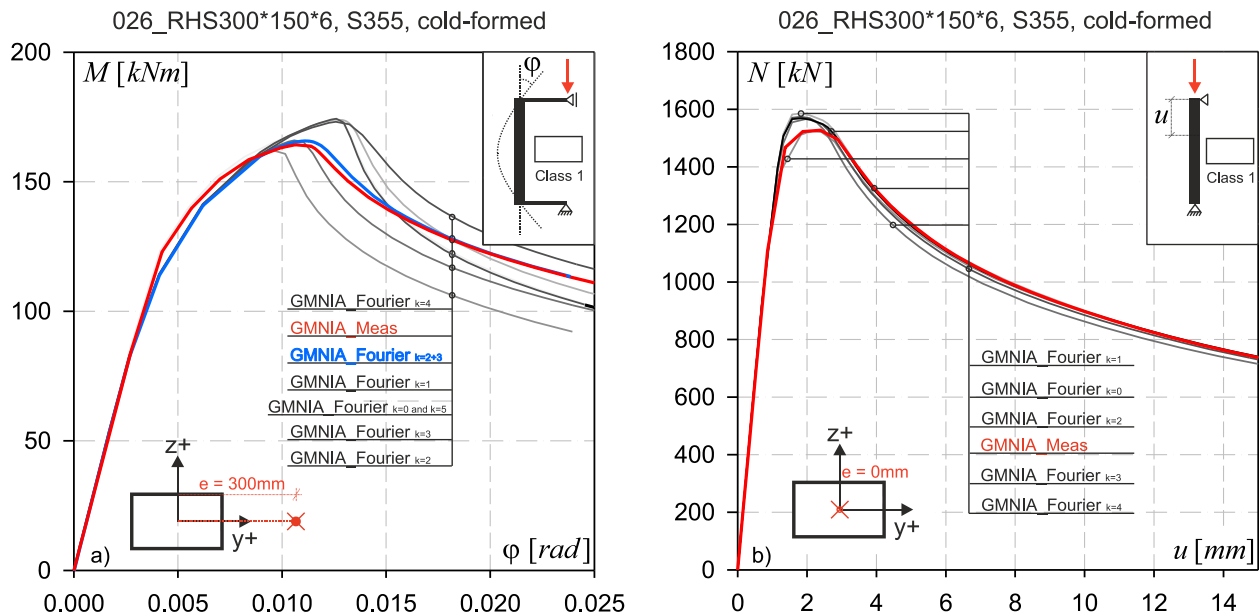

Figure 12: Comparison between individual harmonic numbers for a RHS 300*100*6 profile with a: eccentric load and b: centric load

A similar result compared to that shown in Fig. 10 is obtained. The lowest scatter in the post-buckling behaviour may be assessed for the centric load case (see Fig.12b). This can be attributed to a similar buckling shape in each examined case, even though the location of the buckling field varied along the height of the reconstructed models. This variation makes apparently no big difference in case of centric pressure, as long as the buckling shape (see exemplary Fig.11 bottom) remains mainly the same. The decisive imperfection shape seems to be replicated by the harmonic number of $k = 2$, as its force-displacement-curve has almost the same shape compared to the curve of GMNIA_Meas, regarding the maximum load and the displacement. This leads to the assumption that the indicated harmonic number has a greater dominance over other imperfection shapes, confirming the statement that critical imperfections are not usually those with the largest amplitude, instead those with wavelengths close to the critical buckling mode (Sadowski et.al., 2015).

In case of the eccentric load (see Fig.12a), not only the post-buckling scatter is higher but also significant differences in the rising brunch can be identified, attributed to different imperfection amplitudes associated with individual harmonic numbers. The biggest difference in the post-buckling area is caused by different plastic hinge locations. The lowest moment-rotation relation is calculated for the reconstructed surface with the harmonic number of $k = 2$ and $k = 3$. By summing this "critical" harmonic numbers, an additional surface was reconstructed and calculated (Fig.12a-blue curve), leading to almost the same moment-rotation behaviour compared to the curve of GMNIA_Meas. In the case of eccentric load application two governing harmonic numbers were identified, which describe the moment-rotation relation accurately, leading to the same statement as for the centric load case.

4. Conclusions
This paper presents an in-depth study of the buckling and post-buckling behavior of RHS and SHS hollow sections focusing on the effect of initial imperfections in physical specimens. These were obtained, in a first step, by a 3D-scanning procedure. By using a surface reconstruction method based on a Fourier series expansion, it is possible to evaluate a range of imperfections within one specimen that can be described by harmonic numbers. To confirm the accuracy of the surface reconstruction method by comparing it to the actual scanned geometry, harmonic numbers were taken in an ascending sequence from $k = 0$ to 40, leading to accurate results at an already low harmonic range. Additional GMNIA calculation were performed, using the reconstructed imperfections as a FE-modelling basis. It was shown, that in the case of the centric and eccentric load application the accuracy, regarding the force-displacement and moment-rotation-relation, respectively, increased with higher values of the harmonic number combinations. However, sufficient results regarding the resistance and deformation could be achieved in a lower range between $k = 0$ and $k = 10$. As a final step of the presented paper a "weighting factor", in the sense of a term, was introduced. Therefore, additional calculations were performed by using the harmonic numbers from $k = 0$ to 5 separately to reconstruct, in each case, an imperfect surface based on just one individual harmonic number. Finally, dominant imperfection forms were identified for a RHS profile loaded by two different load cases, a centric and eccentric load application.

A further step towards a slenderness-based deformation and rotation capacity formulation is the expansion of the presented method in this paper on a wider range of tubular hollow cross-sections

e.g. SHS, RHS and CHS profiles based on different manufacturing processes like cold-forming or hot rolling. As the evaluation presented here is based on only a friction of the pool of tested specimens within the framework of the project "HOLLOSSTAB", further research is under way in order to investigate the reconstruction method in a more detailed way. Following up on the work of Cai and Moen (2015), the authors' future research focus will be laid on the derivation of a buckling-mode identification method, where LBA eigenmodes are used to represent crucial imperfections forms, decisive for the buckling behaviour of the specimen or the whole structure under consideration in the pre- and (as was shown in this paper) post-buckling range.

Acknowledgments

References

Abaqus. Refernce manual, version 6.16. (2016). *Simulia, Dassault Systéms*. France.

Abvabi, A. & Rolfe, B. & Hodgson, P.D. & Weiss, M. (2015). "The influence of residual stresses on a roll forming process." *International Journal of Mechanical Sciences* 101-102 (10) 124-136.

Amouzegar, H. & Schafer, B.W. & Tootkaboni, M. (2016). "An incremental numerical method for calculation of residual stresses and strains in cold-formed steel members." *Thin Walled Struct.* 106 (09) 61–74.

Boeraeve, Ph., Lognard, B., Janss, J., Gérardy, J., Schleich, J. B. (1993). "Elasto-plastic behaviour of steel frame works." Journal of Constructional Steel Research, Volume 27, Issues 1-3, pp. 3-21.

Cai, J., Moen, C.D., (2015). "Automated buckling mode identification of thin-walled structures from 3D finite element mode shapes or point clouds." *Proceedings of the Annual Stability Research Council 2015, Nashville, Tennessee.*

DIN EN 1993-1-1. (2005). "Eurocode 3. Design of steel structures – Part 1-1: General rules and rules for buildings." *CEN – European Committee for Standardization.* Brussels.

DIN EN 10210-2. German version EN 10210-2: (2006). "Hot finished structural hollow sections of non-alloy and fine grain steels – Part 2: Tolerance, dimensions and sectional properties."

DIN EN 10219-2. German version EN 10219-2: (2006). "Cold formed welded structural hollow sections of non-alloy and fine grain steels – Part 2: Tolerances, dimensions and sectional properties."

Ding, X., Coleman, R., Rotter, J. M., (1996). "Techniques for precise measurement of large-scale silos and tanks." *Journal of Surveying Engineering,* 122 (1-2) 14-25

Gardner, L. & Saari, N. & Wang, F. (2010). "Comparative experimental study of hot-rolled and cold-formed rectangular hollow sections." *J. of Thin-Walled Structures* 48 (7) 495-507.

Kato, B. (1982). "Cold-formed Welded Steel Tubular Members." *Applied Science Publishers, London, UK.*

Kuhlmann, U. (1989). "Definition of flange slenderness limits on the basis of rotation capacity values." *J. Constr. Steel Res.,* vol. 14, no. 1 pp. 21-40.

Ma, J.-L. & Chan, T.-M. & Young, B. (2015). "Material properties and residual stresses of cold-formed high strength steel hollow sections." *Journal of Constructional Steel Research* 109 (6) 152-165.

McAnallen, L.E., Padilla-Llano, D.A., Zhao, X., Moen, C.D., Schafer, B.W., Eatherton, M.R. (2014). "Initial Geometric Imperfection Measurements and Characterization of Cold-Formed Steel C-Section Structural Members with 3D Non-Contact Measurement Techniques." *Proceedings of the Annual Stability Conference, Structural Stability Research Council* (3), Toronto, Canada

Meng, X., Toffolon, A., Gardner, L., Taras, A. (2019). "The generalised slenderness-based resistance method for the design of CHS and EHS." *Steel Construction,* Vol. 12, Issue 4, Wiley.

Müller, A., Hausmann, B., Taras, A. (2018). "Study on the influence of imperfections and strain hardening on the buckling strength of spiral –welded aluminum circular hollow sections." *Conference paper, Eighth ICTWS 2018* (8), Lisbon.

Müller A., Taras A. (2019a). "Study on the deformation and rotation capacity of HSS beams and beam-columns." *Conference Paper, The international colloquium on stability and ductility of steel structures, September 2019* (9), Prague

Müller A., Taras A. (2019b). "Preliminary study on the impact of initial imperfections on the post-buckling rotation of square hollow sections in uniform bending." *Conference Paper, Nordic Steel Conference 2019* (9), *Copenhagen*

Müller, A., Taras A. (2019c). "On the post-buckling rotational capacity of squared hollow sections in uniform bending. An initial study on the impact of initial imperfections on deformation paths." *Steel Construction – Design and Research* 12, No. 3 (8).

Müller A., Taras A. (2019d) "Imperfection evaluation methods of large scale spiral-welded tubes based on experimental tests and progressive reverse engineering procedures." *Conference Paper, 17th International Symposium on Tubular Structures (12), Singapore*

Ricles, J.M. and Sause, S. and Green, P.S. (1998). "High-strength steel: implications of material and geometric characteristics on inelastic flexural behavior." *Eng. Struct.* 20 (5-6) pp. 323-335.

Sadowski, A.J., Reinke, T., Van Es, S.H.J., Rotter, J.M.,Gresnigt, A.M., Ummenhofer, T. (2015). "Harmonic analysis of measured initial geometric imperfections in large spiral welded carbon steel tubes." *Engineering Structures,* 85C (1) 234-248.

Saloumi, E. (2016). "Development of a new design method to define the rotation capacity of steel hollow sections." *Phd-Thesis*. Liége University, Saint-Joseph University.

Stanghoner, N. and Sedlacek, G. and Boeraeve, P. (1994). "Rotation requirement and rotation capacity of rectangular, square and circular hollow section beams." *Tubular structures VI, Grundy,* Holgate & Wong (eds).

steelconstruct (2019). "Overall-Slenderness Based Direct Design for Strength and Stability of Innovative Hollow Sections." www.steelconstruct.com/eu-projects/hollosstab access Jan. 20, 2020

Teng, J.G., Lin, X., Rotter, J.M., Ding, X.L., (2005). "Analysis of geometric imperfections in full-scale welded steel silos." *Engineering Structures* 27 (1) 938-950.

Toffolon, A., Müller, A., Nico, I. Taras, A. (2019a). "Experimental and numerical analysis of the local and interactive buckling behaviour of hollow sections." *Proceedings of SDSS 2019,* Prague.

Toffolon A., Meng X., Taras A., Gardner L. (2019b). "The generalised slenderness-based resistance method for the design of SHS and RHS." *Steel Construction,* Vol. 12, Issue 4, Wiley.

Toffolon, A., Taras, A. (2019c). "Development of an OIC-Type local buckling design approach for cold-formed unstiffened and groove-stiffened hollow sections." *Thin-Walled Structures,* 144 (6) Elsevier.

Toffolon A., Taras A. (2019d) "Proposal of a design curve for the overall resistance of cold formed RHS and SHS members", *Conference Paper, Nordic Steel Conference 2019,* Copenhagen.

Tong, L. & Hou, G. & Chen, Y. & Zhou, F. & Shen, K. & Yang, A. (2012). "Experimental investigation on longitudinal residual stresses for cold-formed thick-walled square hollow sections." *J. Constr. Steel Res.* 73 (6) 105–116.

Wilkonson, T. (1999). "The Plastic Behaviour of Cold-Formed Rectangular Hollow Sections."

Yun, X. & Gardner, L. (2017). "Stress-Strain curves for hot-rolled steels." *Journal of Constructional Steel Research* 133 (6) 36-46.

Yun, X. & Gardner, L. (2018). "Description of stress-strain curves for cold-formed steels." *Construction and Building Material* 189 (11) 527-538.

Zhang, X.Z. & Liu, S. & Zhang, M.S. & Chiew, S.P. (2010). "Comparative experimental study of hot-formed, hot-finished and cold-formed rectangular hollow sections." *J. of Case Studies in Structural Engineering* 6 (12) 115-129.